Proton Uptake at the Barite−Aqueous Solution Interface: A Combined Potentiometric, Electrophoretic Mobility, and Surface Complexation Modeling Investigation

Michael L. Machesky,* Moira K. Ridley, Frank Heberling, and Johannes Lützenkirchen

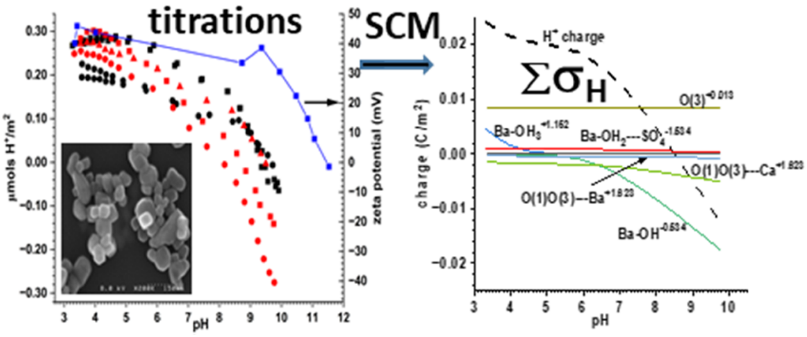

ABSTRACT: A well-characterized barite powder was investigated via base titrations as functions of pH (3 to 10), ionic strength (0.03 and 0.30 m NaCl), and temperature (15 to 50 °C) and with and without added Ca^{2+} (0.001 and 0.002 m), along with ζ-potential measurements (25 °C, pH 2.5 to 11.5 in 0.001 m NaCl). Ba^{2+} concentrations measured in parallel dissolution experiments and Ca^{2+} concentrations measured at the conclusion of titration runs were utilized to constrain solution conditions. X-ray surface diffraction and molecular modeling results for the barite (001) surface from the literature were employed to estimate surface protonation constants via the MUSIC model. This information was integrated into a surface complexation model (SCM) of the barite−aqueous solution interface, with one Helmholtz plane utilized to accommodate Ba^{2+}, Ca^{2+}, and SO_4^{2-} adsorption. Proton uptake/release between pH 3 and 11 was < 0.7 μmols/m², which is approximately 10 times less than for typical metal oxides over the same pH range, while ζ-potentials were similar to metal oxide values. Although H^+ uptake/release exhibited slight differences with respect to ionic strength, temperature, and added Ca^{2+}, these differences could not be confidently differentiated from various sources of experimental error and model uncertainties including pretreatment procedures, blank titrations, or MUSIC model assumptions. Therefore, along with binding constants and a Stern layer capacitance value, the SCM included a "δ" parameter, which allowed for slight vertical adjustments of the individual base titration curves during fitting. As a result, the final model parameters for all titration conditions were very similar.

KEYWORDS: *barite, proton charge, ζ-potential, surface complexation modeling, MUSIC model*

1. INTRODUCTION

The barite−water interface has been subject to considerable scrutiny with a practical motivation being to understand and control scale formation of this relatively low solubility mineral during oil and gas production.[1] Dissolution/precipitation kinetics have been characterized via both macroscopic[2,3] and microscopic[4−8] approaches, with particular focus on the (001) and (210) surfaces which dominate the habit of natural barite crystals.[9] Of greater relevance to the barite−aqueous solution interface are studies which have probed the molecular-level properties of the barite−water interface including interfacial water, surface relaxation, and adsorbed ion structure. Bracco et al.[10] characterized the hydration structure of the barite (001) surface with specular and nonspecular X-ray surface diffraction and molecular dynamics (MD) simulations. Surface displacements of lattice Ba^{2+} and SO_4^{2-} were quantified, as were the configurations of adsorbed water molecules which occupy 4 distinct positions consistent with Ba^{2+} and SO_4^{2-} in the bulk crystal lattice. Synchrotron X-ray surface diffraction and 3 types of molecular modeling methods were used to characterize Sr^{2+} sorption at the hydrated barite (001) surface.[11] Strontium adsorbed in both inner-sphere (IS) and outersphere (OS) fashion and also exchanged for surface Ba^{2+}. Metadynamics simulations also revealed that IS Ba^{2+} adsorption was more exothermic than Sr^{2+} adsorption. Bracco et al.[12] investigated Pb^{2+} sorption at the barite (001) surface with specular resonant anomalous X-ray reflectivity (RAXR). As for Sr^{2+}, both IS and OS adsorption as well as exchange for surface Ba^{2+} occurred, but adsorbed amounts and adsorption isotherm shapes differed, with evidence of surface precipitation at Pb^{2+} concentrations above about 350 μM. As noted by Weber et al.,[13] a robust surface complexation model (SCM) for the barite surface would allow these observations to be incorporated into a predictive framework for ion adsorption by the barite surface.

SCMs were first developed 50 years ago to help rationalize the pH-dependent ion adsorption behavior of hydrous metal oxides.[14,15] Initially, SCMs were generic in nature and based entirely on macroscopic observables such as pH charge titrations, adsorption pH edge experiments, and the like,[16] which resulted in a wide variety of SCM parameters that fit such data equally well.[17] This model ambiguity has been reduced over the last 30 years by the increasing availability of molecular-level information from spectroscopic and atomistic simulation results which have clarified interfacial structures and processes and thereby provided microscopic constraints to model parameters such as adsorption constants.[18] Consequently, SCMs have evolved into a convenient integrative tool with which to interpret ion adsorption at mineral−water interfaces.

Currently, the best examples of the integrative power of SCMs involve prototypical metal oxides such as Fe oxides,[19−21] and Ti oxides,[18,22] for which a wide variety of macroscopic and molecular-level results exist. This is not typically the case for other common mineral−water interfaces including ionic solids such as carbonates and sulfates. The generally higher reactivity (e.g., solubility, dissolution kinetics) of these minerals means conventional acid−base pH titration and ion adsorption data are difficult to correctly collect and interpret.[23−25] As a result, most such studies have relied exclusively on electrokinetic measurements to characterize the pH-dependent behavior of ionic solids such as calcite and to develop SCMs.[26] However, Eriksson et al.[27] performed potentiometric and ζ-potential titrations on calcite suspensions, with NaCl as the background electrolyte. Net proton charge densities increased from about −0.05 to 0 C/m^2 between pH 11 and 8−9, and thereafter increased much more rapidly to about 0.20−0.25 C/m^2 at pH 7.5−7. ζ-Potentials remained positive over the same pH interval, increasing from roughly 10 mV at pH 11 to > 24 mV near pH 9. In a follow-up investigation, Eriksson et al.[28] probed the effect of excess lattice ions (Ca^{2+}, CO_3^{2-}) on proton charge and ζ-potentials. Increasing concentrations of Ca^{2+} (as $CaCl_2$) shifted net proton charge curves in the negative direction between pH 11 and 8, while the opposite was true for excessively added CO_3^{2-} (as Na_2CO_3). Conversely, ζ-potentials became more negative with increasing CO_3^{2-} concentrations. Neither of these studies utilized an SCM to help interpret the results. Villegas-Jiménez et al.[29] performed potentiometric acid−base titrations on gaspeite ($NiCO_3$), a low solubility carbonate mineral which they proposed is a suitable surrogate for more common carbonate minerals such as calcite. Proton uptake between pH 10 and 5 was 4−6 μmol/m^2, and zero net proton charge pH values decreased from 8.7 to 6.3 with increasing background electrolyte concentration (0.001 to 0.1 M NaCl). A one-site 3-pK constant capacitance SCM adequately reproduced the acid−base titration data, although it was acknowledged that some of the fit model parameters such as capacitances were higher (10−15 F/m^2) than physically plausible. Such high capacitance values have been a relatively common feature of carbonate SCMs,[23,30,31] with several more recent exceptions.[32,33]

Available macroscopic studies of barite are limited to ζ-potential measurements in various electrolyte solutions.[34−37] In low ionic strength monovalent electrolyte media (which includes Ba^{2+} and SO_4^{2-} from barite dissolution), these studies reported slightly positive and relatively constant (0 to 25 mV) ζ-potentials below pH 7, which then decreased rapidly to negative values (−25 to −35 mV) at high pH (∼9 to 13). Higher ionic strengths (>10^{-3} M), particularly with divalent ions markedly affected ζ-potentials with respect to pH; carbonate and sulfate solutions resulted in more negative ζ-potentials and calcium and barium solutions yielding more positive ζ-potentials. The role of Ba^{2+} and SO_4^{2-} as potential determining ions for barite was investigated by Bokern et al.[38] via AFM and ζ-potential measurements. Over a narrow range of added Ba^{2+} and SO_4^{2-} concentrations (<10^{-4} M), ζ-potentials varied linearly with log added concentration, corroborating their potential determining role. As far as we are aware, there are no SCMs dealing with barite.

Here, we present base titrations of a well-characterized barite powder as functions of pH (3 to 10), ionic strength (0.03 and 0.30 m NaCl), and temperature (15 to 50 °C) and with and without added Ca^{2+} (0.001 and 0.002 m), along with a set of ζ-potential data (25 °C, pH 2.5 to 11.5 in 0.001 m NaCl). These data along with X-ray surface diffraction and atomistic simulation results for the barite (001) surface from the literature, as well as Ba^{2+} concentrations measured in parallel dissolution experiments and Ca^{2+} concentrations measured at the conclusion of titration runs are then utilized to develop a SCM of the barite−aqueous solution interface.

2. MATERIALS AND METHODS

2.1. Barite Powder. The synthetic barite powder used in this study was obtained from Sachtleben Minerals GmbH, Germany (HU-N Lot 300244374). Prior to use, the barite was washed; washing comprised at least 10 rinsing (distilled−deionized water), heating (50 °C), and decantation cycles. A few titrations on unwashed samples were also performed for comparative purposes. The washing procedure helped ensure that the particle surfaces were free of residue from the synthesis process and likely minimized ultrafine particles and highly reactive defect sites. Regardless, titrations were more reproducible after the cleaning procedure. The barite powders were characterized using X-ray diffraction (XRD), Brunauer−Emmett−Teller (BET) N_2-adsorption surface area measurements, and high-resolution electron microscopy. XRD characterization confirmed that the samples were pure crystalline barite. Imaging results show monodisperse, euhedral grains with visible facets including (001) faces, and an average diameter of about 40 nm (Figure 1). The N_2-BET surface areas of the unwashed and washed powders were 23.1 and 22.1 m^2/g, respectively.

2.2. Experimental Procedures. The potentiometric titration procedure used in this study has been described in detail previously.[39,40] For clarity, an overview of key aspects of the titration procedures are repeated here and additional details are provided as the Supporting Information. All

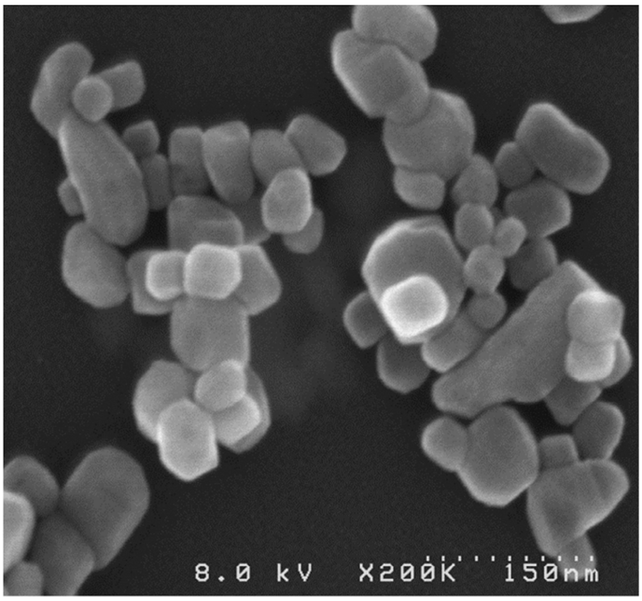

Figure 1. Representative scanning electron micrograph (SEM) of the barite powder used for the proton and ζ-potential titration experiments.

experimental solutions were prepared from reagent-grade chemicals and deionized water. Solutions were prepared in NaCl media, with sufficient electrolyte to produce overall ionic strengths of 0.03 and 0.3 m. The effect of Ca^{2+} on proton uptake was determined with test solutions comprising 0.001 m Ca^{2+} and sufficient NaCl to produce ionic strengths of 0.03 and 0.3 m. Additional experiments were conducted at 0.3 m ionic strength with a test solution containing 0.002 m Ca^{2+}. Ca^{2+} was chosen for study because it is typically the most common divalent cation in natural waters and is expected to interact with the barite surface in some manner.[41] The Ca^{2+} concentrations were purposefully selected to ensure undersaturation with respect to both gypsum and anhydrite throughout the titration procedure. PHREEQC 3[42] simulations revealed that saturation indexes for both gypsum and anhydrite were always <-3.

For all titrations, a Mettler autotitrator and Ross semimicro combination glass electrode were used. The electrode was calibrated using an initial base solution, to which an acid was added giving a second calibration point. The barite titrations were performed by suspending ~0.65 g of barite in ~40 g of test solution. The titration cell was immersed in a water bath at the desired temperature (15, 25, 35, or 50 °C), the headspace was purged with purified argon to prevent CO_2 contamination, and the solution was stirred mechanically throughout the experiment. During each experiment, 15−25 aliquots of base titrant were added over a pH_m range of approximately 7 units (where pH_m is moles H^+ per kg solution). Similarly, to ensure CO_2 free solutions, all base titrants were purged with purified argon and stored under a positive-pressure argon atmosphere. All titrations were completed in under 4 h. At the termination of titrations with Ca^{2+}, a sample was withdrawn, filtered through 0.2 μm PVDF membrane filters into preweighed polypropylene syringes containing a known amount of high-purity 1 m HNO_3. The samples were later analyzed for total dissolved Ba^{2+} and Ca^{2+} concentrations by inductively coupled plasma atomic emission spectroscopy (ICP-AES).

From the titrations, net proton adsorption (desorption), expressed as an excess or deficit of micromole H^+ per square meter of surface area, was obtained for each titration point. Consequently, a single set of acid-to-base titration data was obtained from each potentiometric titration. Duplicate titrations were conducted at 25 °C to help assess data uncertainty. Data reduction of the titration results followed standard procedures detailed in Ridley et al.[39]

Proton adsorption by barite was small, making the titration measurements quite sensitive to small errors from minor protolytic impurities. Therefore, we conducted background titrations at each temperature and ionic strength. Background titrations were performed following the same procedure and using the same test and titrant solutions but with no barite in the titration cell. The values of excess or deficit H^+ in these background titrations were used to correct the concentration of calculated H^+ in the barite experiments. This correction is also referred to as a "solution blank" correction.

Although the solubility of barite is relatively low ($K_{SP} = 10^{-9.97}$ at 25 °C),[43] there was dissolution of the barite over the course of the titrations. Consequently, we measured the dissolution of barite over several hours, equivalent to the duration of the titrations. The solubility experiments were conducted with identical solid-to-solution ratios as used for the titrations, and followed the same protocol. Solutions were prepared at three pH values (3, 4.5, and 5.5) and with sufficient NaCl to give 0.3 m ionic strength. The acidic pH and high ionic strength conditions were selected so as to maximize possible barite dissolution. Experiments were performed at 15, 25, and 50 °C, and samples were withdrawn from the test solutions after 1, 3, and 5 h. Filtering, acidification, and later analysis of the samples followed the approach described for the Ca^{2+} titrations.

ζ-Potentials were measured on 200 mg/L barite suspensions with a Brookhaven NanoBrook 90plus PALS instrument. Separate suspensions at various pH values were equilibrated under an argon atmosphere in 1 mM NaCl solution for at least 2 weeks prior to ζ-potential measurements. Error was assessed from 5−10 measurements on separate aliquots at each pH value. Shorter equilibration times, including experiments with the addition of Ba^{2+} and SO_4^{2-} to help attain solubility equilibrium, resulted in significant pH drift, particularly between pH 4 and 9, and irreproducible ζ-potential measurements. Measurement attempts at temperatures other than 25 °C also resulted in erratic ζ-potential results. Ultimately, only 25 °C results on suspensions equilibrated for at least 2 weeks were used for SCM calibration.

2.3. Modeling.

Model fits were determined with the aid of the custom graphical user interface P^3R,[33] a Python based optimization software employing PhreeqC 3[42] via Phreeqpy (https://phreeqpy.com/). The optimization routine minimizes a normalized χ^2 function

$$\chi^2 = \frac{1}{n-b}\sum_{i=1}^{n}\left(\frac{y_{i,\mathrm{exp}} - y_{i,\mathrm{model}}}{y_{i,\mathrm{err}}}\right)^2 \tag{1}$$

where n is the number of data points, b the number of adjusted parameters, and y_{exp}, y_{err}, and y_{model} are experimental values, their uncertainty, and the corresponding calculated value, respectively. The optimization was performed via a Nelder−Mead simplex algorithm. A Levenberg−Marquardt algorithm can be applied as well. Parameter uncertainties are estimated

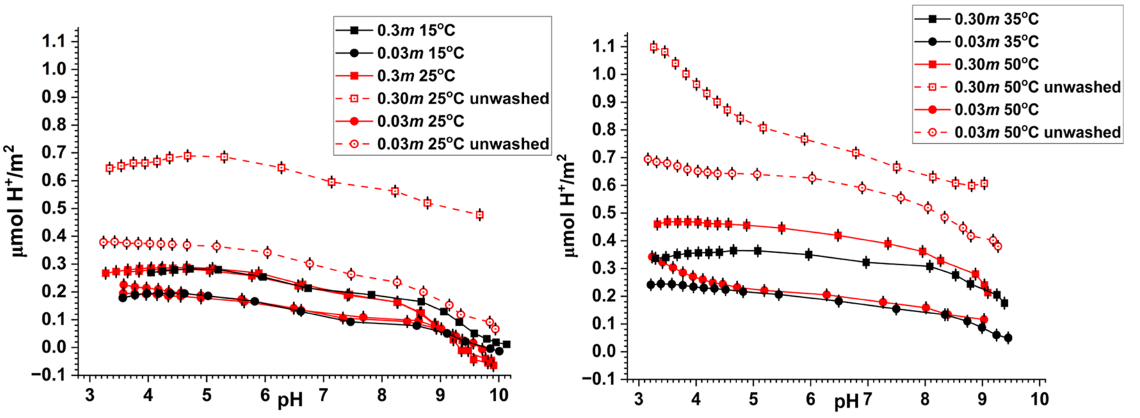

Figure 2. Net proton adsorption data at 15 and 25 °C (left) and 35 and 50 °C (right) in 0.03 m (circles) and 0.30 m NaCl (squares). Experimental conditions are given in the figure legends. Error bars signify titration cure reproducibility (±0.02 μmol H^+/m^2).

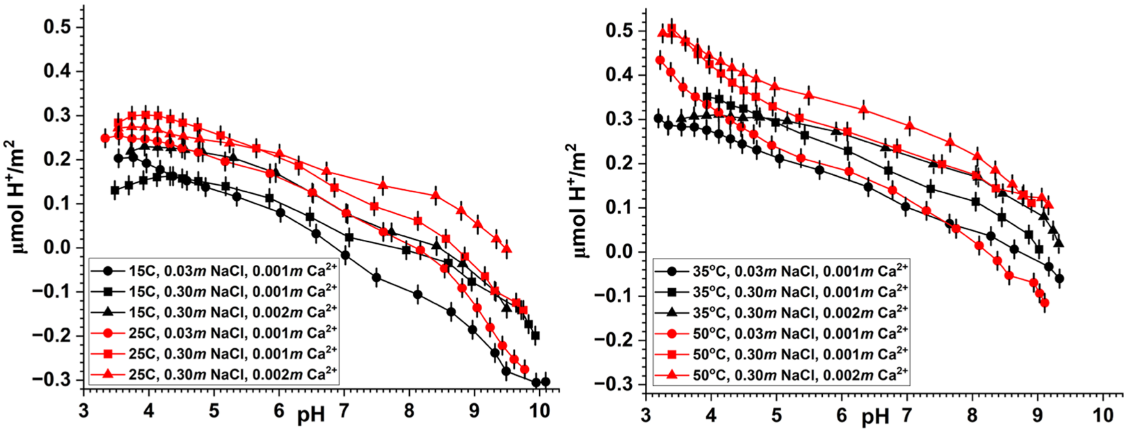

Figure 3. Net proton adsorption data in the presence of Ca^{2+} at 15 and 25 °C (left) and 35 and 50 °C (right). Experimental conditions are given in the figure legends. Error bars are ± 0.02 μmol H^+/m^2.

on the basis of "scaled sensitivities" of each adjustable parameter (with value p) on each datapoint. In short, scaled sensitivities are written to the ($b \times n$) matrix $\boldsymbol{X}$, with indices $i = 1 \cdots n$ and $j = 1 \cdots b$

$$x_{i,j} = \frac{\frac{\partial y_{i,\text{model}}}{\partial p_j} \cdot p_j}{y_{i,\text{err}}} \qquad (2)$$

A centered differencing scheme is used to calculate the partial derivatives (unless the parameter value is at its specified limit). Data weights are written to an ($n \times n$) matrix $\boldsymbol{W}$, where $w_{i,i} = (1/y_{i,\text{err}})^2$ and all other entries are zero. The two matrices $\boldsymbol{X}$ and $\boldsymbol{W}$ allow for a straightforward calculation of a covariance matrix, $\boldsymbol{V}$

$$\boldsymbol{V} = \chi^2(\boldsymbol{X}\cdot\boldsymbol{W}\cdot\boldsymbol{X}^T)^{-1} \qquad (3)$$

The procedure is adopted from the USGS inverse modeling software UCODE.[44] $\boldsymbol{V}$ is then further used to calculate parameter standard deviations and correlation coefficients. A nice feature of P^3R is that scaled sensitivities may easily be visualized together with data and fits and provide valuable information on parameters particularly sensitive to fitting certain parts of the data. All titrations at each temperature (including ζ-potentials at 25 °C) were fit together using the minteqv4.dat thermodynamic database.

3. RESULTS

3.1. Proton Adsorption and ζ-Potential Titrations. Net proton adsorption curves (expressed as excess/deficit μmol H^+/m^2) of barite from 15 to 50 °C in NaCl media are shown in Figure 2, with the results at 25 and 50 °C including data from experiments with both washed and unwashed barite. Titration curve reproducibility (±1 SD) is estimated to be 0.02 μmol H^+/m^2 from duplicate titrations. Notably, proton release between pH 3 and 10 is minimal (<0.35 μmol H^+/m^2), and duplicate titrations (at 25 °C) show relatively small differences (<0.04 μmol H^+/m^2), especially at the low pH start of the titrations. Unwashed sample curves are similar in shape to those of the washed samples but are displaced to higher μmol H^+/m^2 values. The curves are relatively flat between pH 3 and 8 (except for the curve at 50 °C in 0.03 m NaCl) and then decrease more rapidly. Net proton adsorption is always positive at 35 and 50 °C but decreases to small negative values above pH 9.5 at 15 and 25 °C for the washed samples. The 15 and 25 °C curves are very similar in magnitude, as are the 35 and 50 °C curves in 0.03 m NaCl except below pH 4.

Figure 3 shows the net proton adsorption on barite samples in the presence of 0.001 m Ca^{2+} in 0.03 and 0.3 m NaCl and 0.002 m Ca^{2+} in 0.3 m NaCl. Starting μmol H^+/m^2 values near pH 3 are similar to those for washed samples in Figure 2 (0.2–0.5 μmol H^+/m^2), but the slopes of the curves above pH 5 are noticeably steeper and most curves attain negative μmol $H^+/$

m^2 values. The 15 and 35 °C curves are generally lower in magnitude than those at 25 and 50 °C, respectively.

Figure 4 shows proton adsorption isotherms with and without Ca^{2+} present at 25 °C and also ζ-potential data obtained in 0.001 m NaCl. The shape of the ζ-potential curve is similar to that of the proton titration curves in the absence of added Ca^{2+}, that is, ζ-potential values are relatively constant at 0.03 to 0.04 V below pH 9 and then decrease rapidly to an apparent pH_{iep} (isoelectric or zero ζ-potential value) of 11.5.

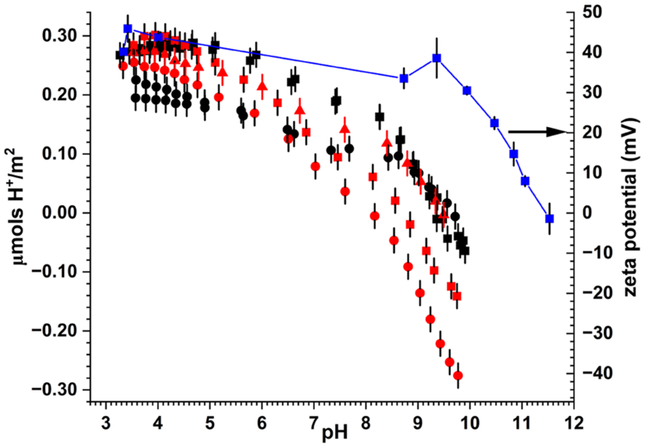

Figure 4. Net proton adsorption (left axis) and ζ-potential (right axis) data at 25 °C. Experimental conditions are given in the figure legends. Error bars signify ± 1 SD titration data reproducibility.

3.2. Barite Solubility. The solubility experiments were not designed to evaluate the equilibrium solubility of barite, as there are well accepted studies and values. Rather, the intent was to measure the degree of barite dissolution that would occur over the course of the titrations. The dissolution of barite after 3 h in 0.30 m NaCl at 25 and 50 °C, depicted as solution Ba^{2+} concentrations, is shown in Figure 5, which also includes the concentration of dissolved Ba^{2+} measured after completing the acid-to-base titrations (pH > 8.5 values). The results reflect decreasing dissolution kinetics with pH and increasing dissolution (solubility and kinetics) with temperature.

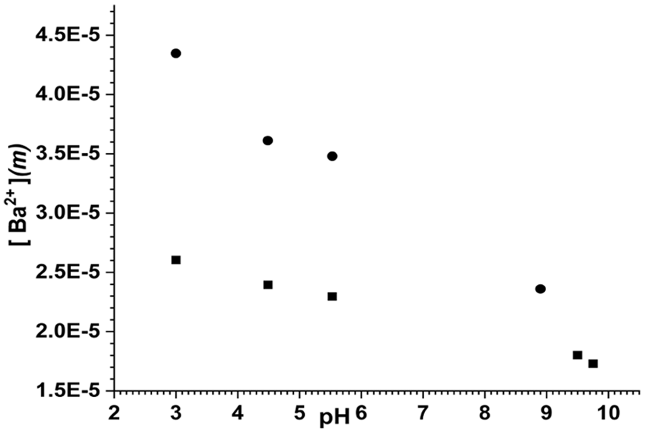

Figure 5. Solution Ba^{2+} concentration vs pH after 3 h in 0.30 m NaCl at 25 °C (squares) and 50 ° C (circles).

3.3. Barite (001) Surface MUSIC Model. The (001) plane is the predominant cleavage surface of barite and is also exposed on the barite powder used in this study (Figure 1). Consequently, the initial step in our modeling efforts was to characterize the possible H^+ adsorption sites of the (001) surface and in particular estimate the protonation constants of those sites utilizing the MUSIC Model.[45]

In bulk barite, barium is 12-fold coordinated by oxygen, sulfur is 4-fold coordinated by oxygen, and each oxygen is coordinated to 3 barium and 1 sulfur. With Ba−O and S−O bond length data from Jacobsen et al.,[46] bond valence (BV) values for Ba−O and S−O bonds were calculated via[47]

$$\mathrm{BV} = e^{(R_o - R)/0.37} \tag{4}$$

where R_o values for Ba and S are reference Ba−O and S−O bond lengths, R for Ba and S are actual Ba−O and S−O bond lengths, and 0.37 is an empirical constant. The R_o bond lengths were adjusted (to 2.247 and 1.626 Å for Ba−O and S−O, respectively) so that BV values for oxygen bonds to Ba and S totaled to 2.0 and 6.0, respectively, as expected for bulk barite.

Forming the (001) surface results in Ba, O, and S atoms existing in nonequivalent high and low positions, with Ba and O being under-coordinated with respect to the bulk. Ba high and Ba low sites are coordinated by 9 and 11 O atoms, respectively, and 3 types of O atoms are 3-fold coordinated to 2 Ba and 1 S atom. O(1) atoms are coordinated to 2 Ba low and 1 S high atom, O(2) atoms are coordinated to 2 Ba high and 1 S high atom, and O(3) atoms are coordinated to 1 Ba high, 1 Ba low, and 1 S low atom. Consequently, there are 5 possible proton reactive sites on the (001) surface, 2 Ba sites which can coordinate water molecules and 3 O atoms which can potentially coordinate protons. These surface groups are illustrated in Figure 6. The densities of these sites are 2.06/nm² for Ba high, Ba low, O(1), and O(2) atoms and 4.12/nm² for the O(3) atom on the (001) surface.

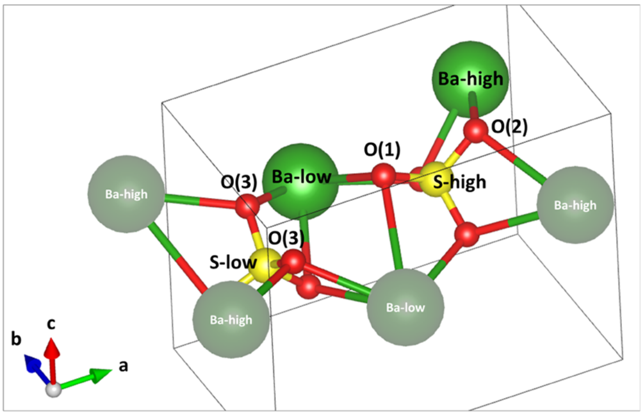

Figure 6. Barite (001) surface groups. Only the top monolayer is shown. Gray shaded atoms are outside the unit cell and shown only to highlight the bonding environment.

Protonation constants at 25 °C were estimated following the MUSIC model,[45] as modified by Machesky et al.[48,49]

$$\log K_{\mathrm{H,T}} = -A_{\mathrm{T}}\left(V + \sum s_{\mathrm{cat-O}} + \sum \mathrm{ms}_{\mathrm{D}} + \sum \mathrm{ns}_{\mathrm{A}}\right) \tag{5}$$

where A_T = temperature-dependent regression constant (21.7 at 25 °C), V = oxygen valence (−2), $\Sigma s_{\text{cat-O}}$ = BV sum of cation−oxygen bonds (Ba−O and S−O here), Σms_D = BV sum of donating H-bonds to adsorbed H_2O (s_D = 0.8), and

Σns_A = BV sum of accepting H-bonds from adsorbed H_2O (s_A = 0.2)

Ba−O and S−O bond lengths were taken from CrystalMaker files (kindly provided by J.N. Bracco, Queens College, City Univ. of NY) prepared from the X-ray reflectivity measurements of the hydrated barite (001) surface in Bracco et al.[10] The bonding configuration of adsorbed water molecules (numbers and lengths of donating and accepting H-bonds) were assumed to equal the default values provided in Hiemstra et al.[45] since the Bracco et al.[10] X-ray reflectivity data do not include information about actual H-bond configurations.

The estimated relevant protonation reactions and constants are given in Table 1.

Table 1. Barite (001) Surface Protonation Reactions and MUSIC Model Estimated Constants

protonation reaction	log K
[a]$\text{Ba–OH}^{-0.848} + H^+ = \text{Ba–OH}_2^{+0.152}$ (Ba low)	18.40
$\text{Ba–OH}_2^{+0.152} + H^+ = \text{Ba–OH}_3^{+1.152}$ (Ba low)	5.38
$\text{Ba–OH}^{-0.534} + H^+ = \text{Ba–OH}_2^{+0.466}$ (Ba high)	11.58
$\text{Ba–OH}_2^{+0.466} + H^+ = \text{Ba–OH}_3^{+1.466}$ (Ba high)	−1.44
[b]$\text{O(1)}^{-0.390} + H^+ = \text{O(1)H}^{+0.610}$	−0.22
[b]$\text{O(2)}^{-0.193} + H^+ = \text{O(2)H}^{+0.807}$	−4.50
[b]$\text{O(3)}^{+0.013} + H^+ = \text{O(3)H}^{+1.013}$	−8.96

[a] The group charge is given by $V + \Sigma s_{\text{cat-O}} + 1$ for each H atom in the group. [b] The number H-bonds accepted by these groups is assumed to be 2.

Note that the Ba high and Ba low groups are positively charged over the accessible pH range, while the O(1) and O(2) groups are unprotonated and negatively charged, and the dominant O(3) group is nearly uncharged. Over our experimental pH range (∼3 to 11), only the $\text{Ba–OH}_2^{+0.152}$ and $\text{Ba–OH}^{-0.554}$ groups would be expected to exhibit significant pH-dependent charging behavior.

3.4. Surface Complexation Model. SCM development was guided by available synchrotron X-ray surface diffraction results and molecular simulations focused on Sr^{2+} adsorption and incorporation at the aqueous barite (001) surface.[11] Strontium was found to be adsorbed as mono- and bidentate IS, as well as OS species, and also incorporated in the barite surface via exchange with Ba^{2+}. Although our charge titrations did not include Sr^{2+}, we assumed that both Ba^{2+} and Ca^{2+} would partition similarly at the interface. The electrical double layer was modeled via the basic Stern formalism with the surface plane reserved for H^+ adsorption (Table 1) and the Helmholtz plane accommodating interfacial Ba^{2+}, Ca^{2+}, and SO_4^{2-}. Additionally, within the diffuse layer which begins at the Helmholtz plane, a "slipping plane" is situated whose distance from the Helmholtz plane was a parameter used to fit the ζ-potential data.[50,51]

Background electrolyte ion adsorption on the barite surface was considered, but preliminary modeling efforts found that inclusion of binding constant parameters for Na^+ and Cl^- did not significantly improve fits. Hence, they were not included in our final fits to reduce model ambiguity. Moreover, various combinations of mono- and bidentate adsorbed configurations to O(1), O(2), and O(3) surface groups for Ba^{2+} and Ca^{2+} resulted in virtually identical fits to our proton adsorption titrations. Consequently, a bidentate IS adsorption complex characterized by Bracco et al.[11] was chosen to exclusively represent Ba^{2+} and Ca^{2+} adsorption to reduce model ambiguity

$$\begin{aligned}&\text{O(1)}^{-0.390} + \text{O(3)}^{+0.013} + \text{Ba}^{2+}(\text{Ca}^{2+})\\&\quad = \text{O(1)O(3)—Ba}^{2+}(\text{Ca}^{2+})^{+1.623}\ K_{\text{bi Ba(Ca)}}\end{aligned} \tag{6}$$

Spectroscopic or molecular simulation constraints on the nature of SO_4^{2-} binding at the barite surface are lacking. Therefore, we assumed that SO_4^{2-} adsorption occurred on protonated forms of the Ba high and low groups, each with the same binding constant

$$\text{Ba–OH}_2^{+0.152} + SO_4^{2-} = \text{Ba–OH}_2 \cdots SO_4^{-1.848}\ K_{SO_4} \tag{7}$$

$$\text{Ba–OH}_3^{+1.152} + SO_4^{2-} = \text{Ba–OH}_3 \cdots SO_4^{-0.848}\quad K_{SO_4} \tag{8}$$

$$\text{Ba–OH}_2^{+0.466} + SO_4^{2-} = \text{Ba–OH}_2 \cdots SO_4^{-1.534}\ K_{SO_4} \tag{9}$$

The solution Ba^{2+} concentrations vs pH results for 0.3 m NaCl presented in Figure 5 were used to help constrain the dissolved Ba^{2+} and SO_4^{2-} concentrations available for adsorption. As an approximation, a barite saturation index of −0.5 was used to set initial dissolved Ba^{2+} and SO_4^{2-} concentrations for all titration conditions. Note that these concentrations are temperature- and ionic strength-dependent. Ideally, dissolved Ba^{2+} and SO_4^{2-} concentrations should both be monitored during future titrations to obtain better constrained solution conditions for model adjustment.

Fitting was accomplished by minimizing the normalized χ^2 function (eq 1) between the experimental and modeled H^+ charge/m^2 and experimental and modeled ζ-potentials. Proton charge (C/m^2) is obtained from μmol H^+/m^2 via multiplication by the Faraday constant.

Fitting parameters included the Helmholtz layer capacitance value, binding constants for Ba^{2+}, Ca^{2+}, and SO_4^{2-}, and a "δ" value, which allowed for slight vertical adjustments of the individual titration curves. We also allowed the protonation constants for Ba (high)$-\text{OH}^{-0.534}$ and Ba (low)$-\text{OH}_2^{+0.152}$ to vary from their MUSIC model estimated values in Table 1 above to improve fits.

Fitting the ζ-potential data also required an additional fitting parameter, the slip plane distance (D_s),

$$\zeta = (4RT/F)\text{arc tanh}[\tanh[(F\psi_d)/4RT]\exp(-\kappa D_s)] \tag{10}$$

where ζ = zeta potential (V), R, T, and F are the gas constant, temperature (K), and Faraday constant, respectively, ψ_d is the potential at the head end of the diffuse layer, and κ is the inverse Debye length.

This approach to fitting ζ-potential data has been utilized in several previous publications,[51−53] although the physical meaning of the slip plane itself is uncertain.[54] Fit parameter values and their standard deviations are summarized in Table 2.

Titrations at each temperature and with and without added Ca^{2+} were fit together in iterative fashion with the aim of maximizing consistency among fitted parameters. Since more titration data were available at 25 °C than at the other temperatures, those results were fit first with all parameters listed in Table 2 allowed to freely vary. Thereafter, except for the δ values, it was determined that parameters at the other temperatures could be constrained near those at 25 °C with

Table 2. Best Fit Parameter Values[a]

						log K								
temp	NaCl (m)	Ca^{2+} (m)	δ	δ SD (C/m^2)	stern cap (F/m^2)	BaOH high	$BaOH_2$ low	Ba^{2+} ads	Ca^{2+} ads	SO_4^{2-} ads	DS (nm)	χ^2	Ca^{2+} measured (mol/m^2)	Ca^{2+} modeled (mol/m^2)
15	0.3	0	0.00894	0.00049										
15	0.03	0	0.00087	0.00494										
15	0.03	0.001	−0.0096	0.00043	0.22 (0.0003)	10.30 (0.0002)	3.97 (0.0005)	4.00 (0.0020)	3.10 (0.0016)	1.19 (0.0204)		3.94	2.25×10^{-7}	1.60×10^{-7}
15	0.3	0.001	−0.0071	0.0005										1.91×10^{-7}
15	0.3	0.002	−0.0013	0.0026									4.64×10^{-8}	2.34×10^{-7}
25	0.3	0	0.00403	0.00062										
25	0.03	0	−0.0007	0.0032										
25	0.001	0	0	0	0.26 (0.0003)	10.51 (0.0002)	4.03 (0.0001)	4.21 (0.0003)	3.1 (0.0388)	1.74 (0.0001)	5.71 (0.1504)	4.98		
25	0.03	0.001	−0.0048	0.00054									2.04×10^{-7}	1.37×10^{-7}
25	0.3	0.001	0.00054	0.00508									1.07×10^{-8}	1.70×10^{-7}
25	0.3	0.002	0.00332	0.00087									1.56×10^{-7}	2.20×10^{-7}
35	0.3	0	0.01335	0.00028										
35	0.03	0	0.00155	0.00242										
35	0.03	0.001	0.00068	0.0045	0.22 (0.0006)	10.78 (0.0002)	3.97 (0.0006)	4.00 (0.0026)	3.1 (0.0002)	1.52 (0.0073)		3.52	2.30×10^{-7}	1.27×10^{-7}
35	0.3	0.001	0.00557	0.00049									5.93×10^{-8}	1.73×10^{-7}
35	0.3	0.002	0.00677	0.00043									1.39×10^{-7}	2.40×10^{-7}
50	0.3	0	0.02035	0.00019										
50	0.03	0	0.00319	0.00138										
50	0.03	0.001	0.0024	0.0014	0.26 (0.0003)	10.20 (0.0006)	4.43 (0.0003)	4.00 (0.0007)	3.1 (0.0388)	1.43 (0.0004)		4.01	1.60×10^{-7}	1.21×10^{-7}
50	0.3	0.001	0.01228	0.00027									7.88×10^{-8}	1.48×10^{-7}
50	0.3	0.002	0.01568	0.00022									4.28×10^{-7}	2.12×10^{-7}

[a] χ^2 is a goodness of fit measure (smaller is better). δ standard deviations (SD) are given in the 4th column and below other parameter values (in parentheses). The last 2 columns give the measured and modeled adsorbed Ca^{2+} concentrations at the end of titrations as determined by difference (added − measured) and converted to mol/m^2 units.

minimal change in goodness of fit as determined by χ^2 values. Consequently, this fitting strategy was followed at all other temperatures to reduce model ambiguity.

Most δ values are positive (except and 15 °C) and are generally greater at 35 and 50 °C than at lower temperatures. Stern layer capacitance values are slightly variable around 0.25 F/m^2. Fit protonation constants for BaOH low and Ba−OH$_2$ high exhibit (+/−) 0.5 log unit variability and are uniformly lower by up to 1.5 log units than their MUSIC model estimates given in Table 1. The Ca^{2+} binding constant was fixed at 3.1 for the final SCM fits in order to ensure that the modeled adsorbed Ca^{2+} concentrations were in reasonable agreement with those measured at the end of the titrations. Protonation constants for BaOH low, Ba−OH$_2$ high, O(1), O(2), and O(3) groups were fixed at their MUSIC-estimated values given in Table 1.

Model fits for the 25 and 50 °C data are presented in Figures 7−10. The complete set of experimental data and model fits are provided as research data. Model fits for the 25 °C data without added Ca^{2+} are presented in Figure 7. Fits to the H$^+$ charge data are best between pH 4 and 8, while the ζ-potential data are best fit near pH 4 and again near pH 11, although above pH 9, the slope of the modeled curve is much shallower than for the experimental data. The fit slip plane distance of 6 nm is near that predicted (~7.5 nm) at 1 mM ionic strength from the empirical relationship between ionic strength and slip plane distance established by Hiemstra et al.[50] Fits to the 25 °C data with added Ca^{2+} (Figure 8) are best for the 0.001 m added Ca^{2+} in 0.3 m NaCl data. Conversely, modeled and measured end of titration Ca^{2+} concentrations are most disparate for that data set.

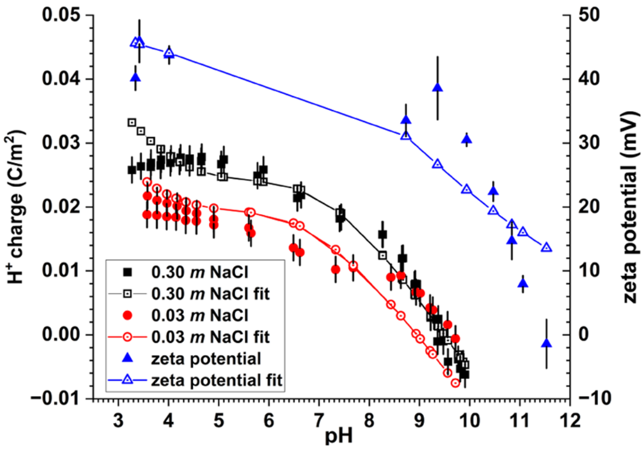

Figure 7. 25 °C without added Ca^{2+} net proton adsorption (left axis) data (0.03 m NaCl closed circles; 0.30 m NaCl closed squares), ζ-potential (right axis) data in 0.001 M NaCl (closed triangles), and corresponding SCM fits (lines and open symbols).

Fits to the 50 °C data without added Ca^{2+} (Figure 9) are best above pH 5 for the 0.30 m NaCl data and below pH 7 for the 0.03 m NaCl data. Fits with the δ values subtracted are nearly identical. Fits to the 50 °C data with added Ca^{2+} (Figure 10) are best for the 0.002 m added Ca^{2+} in 0.30 m NaCl data. PhreeqC 3 input scripts to generate fits to the 25 °C H$^+$ charge and ζ-potential data with and without added Ca^{2+} are provided as the Supporting Information.

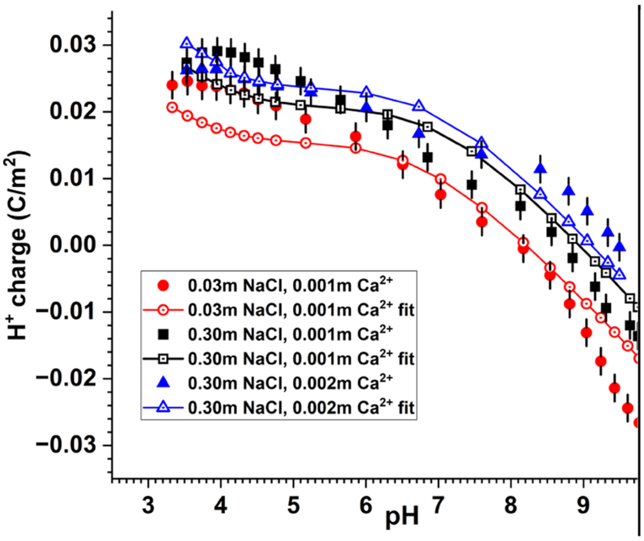

Figure 8. 25 °C with added Ca^{2+} net proton adsorption data (closed symbols) and SCM fits (lines and open symbols). 0.03 m NaCl and 0.001 m Ca^{2+} (circles), 0.30 m NaCl and 0.001 m Ca^{2+} (squares), and 0.30 m NaCl and 0.002 m Ca^{2+} (triangles).

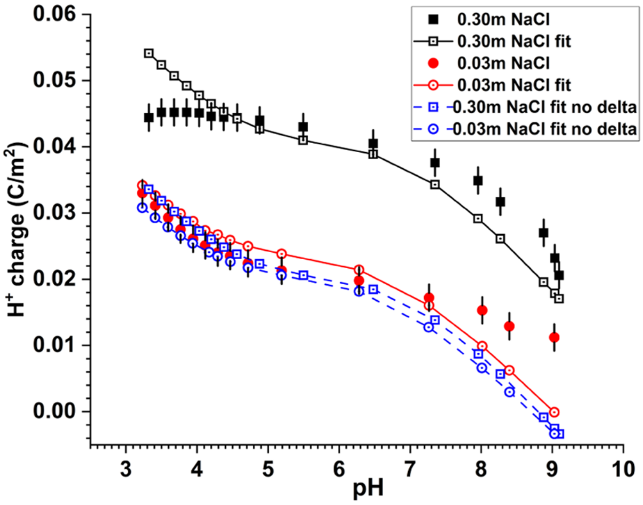

Figure 9. 50 °C without added Ca^{2+} data (closed symbols) and SCM fit (lines and open symbols). 0.03 m NaCl (red, circles) and 0.30 m NaCl (black, squares). The blue curves represent the fits with the δ values subtracted.

4. DISCUSSION

Proton uptake by barite is approximately 10-fold less than on representative metal oxides over the pH range 3−10.5 as depicted in Figure 11. In fact, barite proton uptake is similar to that observed for inert surfaces such as Teflon.[55] Moreover, there are very few proton uptake data sets available for ionic solids to compare with and none for barite. The calcite proton charge curves of Eriksson et al.[27] increase from about −0.025 C/m^2 at pH 10 to 0 C/m^2 at pH 8.5, which is similar to the 0.02 C/m^2 increase for our curves over the same pH interval (Figure 7). At lower pH, however, their calcite proton charge curves increase rapidly to about 0.2 C/m^2 at pH 7.5 (near the endpoint of their titrations), while our curves plateau at 0.02−0.03 C/m^2 near pH 4. It is conceivable that calcite dissolution and the formation of HCO$_3^-$ after the release of lattice CO$_3^{2-}$ is responsible for some of the increase in H$^+$ charge they

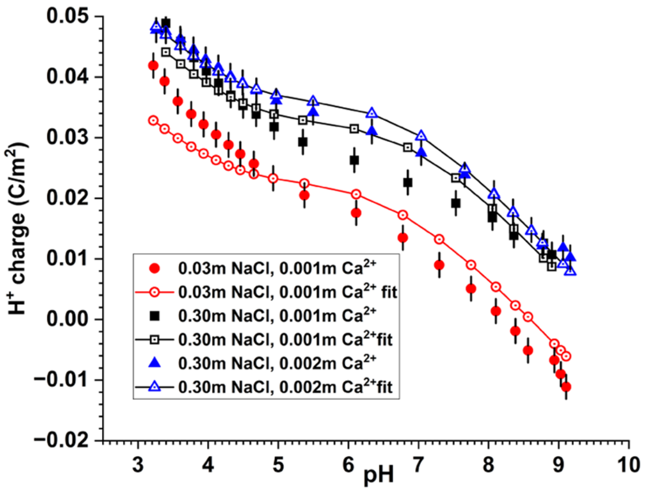

Figure 10. 50 °C with added Ca^{2+} net proton adsorption data (closed symbols) and SCM fit (lines and open symbols). 0.03 m NaCl (circles), 0.30 m NaCl (squares), and 0.002 m Ca^{2+} (triangles).

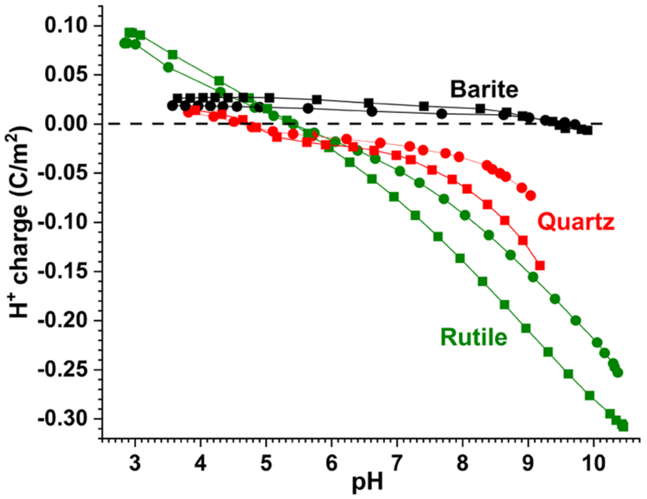

Figure 11. Barite (black), quartz (red), and rutile (green) proton charge data in 0.03 m (circles) and 0.30 m NaCl (squares).

observed below pH 8.5. The proton charge curves of gaspeite ($NiCO_3$) determined by Villegas-Jiménez et al.[29] have shapes analogous to our own, that is, relatively pH-independent below about pH 8 and then much steeper at higher pH values. However, there are two major differences between our data and theirs. First, their proton adsorption densities are roughly 10 times higher than those observed in this study and hence on par with metal oxide values. Second, their data were greatly affected by ionic strength with apparent pH_{znpc} values decreasing from about 8.8 to 7.8 and 6.2 in 0.001, 0.01, and 0.1 M NaCl, respectively. In contrast, our data are less affected by ionic strength, with the largest differences exhibited by the NaCl only data, especially at higher temperatures and for the unwashed samples (Figure 2).

In contrast, our ζ-potential curve is similar in magnitude to those of both metal oxides,[39,50] carbonates,[29,30,56] and previous barite studies.[34] This similarity has its origins in the strongly ordered fluid structure (water + ions) which exists within 15−20 Å of most mineral surfaces.[57] On inert surfaces (encompassing PTFE, diamond, ice, oil) in the presence of aqueous electrolyte solutions, it has also been observed that the interface takes up proton related charge of about one-tenth of typical oxide values, while ζ-potentials are similar.[53,58] SCMs are able to handle all of these cases with consistent sets of parameters. Systems with low "fundamental" charge due to interactions with protons/hydroxide ions invariably exhibit appreciable electrokinetic potentials, which are in the present case within the model simulations.

The low extent of proton uptake by barite means that best practice experimental protocols advocated for metal oxide potentiometric titrations such as pretreatment procedures and blank corrections take on added significance.[59] Titration curves for the unwashed samples are displaced to higher μmol H^+/m^2 values relative to the washed samples (Figure 2). The BET surface area of the unwashed sample is about 5% greater than that of the washed sample suggesting some removal of fines or annealing occurred during the washing procedure. However, that difference is too small to account for the degree of displacement. Notably, the unwashed and washed sample titration curves generally have the same shape and proton uptake over a comparable pH range. This suggests that an acidic impurity was released when the unwashed sample was added to solution, which is responsible for the positive displacement observed. Therefore, adjusting the unwashed curves vertically downward (i.e., along the $\mu mol/m^2$ axis) brings them into closer agreement with the washed samples. Although our pretreatment washing procedure was extensive (at least 10 washing−decantation cycles at 50 °C), it is conceivable that it was incomplete, and consequently the small differences observed between individual titration curves with respect to ionic strength and temperature are due more to differences in acidic impurity levels than inherent ionic strength and temperature effects. That the ionic strength differences were larger at 35 and 50 °C than at lower temperatures supports this possibility. Additionally, solution blank corrections are 20−30% of the measurements themselves at the low pH start of the titrations, which contributes to the uncertainty in precisely locating the initial adsorbed H^+ amount. In fact, low pH solution blank corrections are likely responsible for the decrease in proton adsorption for some titration curves at low pH (e.g., Figure 3). The uncertainty in locating the initial adsorbed H^+ value led us to include a δ parameter within our SCM which allows vertical adjustments to individual titration curves during the fitting procedure. In effect, H^+ charge values are treated as relative rather than absolute quantities.

Our fitting strategy involved fitting all data at each temperature together. As might be expected, fitting each ionic strength data set with and without added Ca^{2+} at each temperature separately resulted in better individual fits but at the expense of much greater parameter variability and hence model ambiguity. For example, at 25 °C best fit, Stern layer capacitance values varied from 0.1 to 0.6 F/m^2, and best fit $BaOH_2^{+0.446}$ protonation constants ranged from 3.4 to 5.1 after fitting each data set separately. Moreover, there was no discernible pattern in fit parameters with respect to either ionic strength or temperature in the individual curve fits. As a result, even when allowing δ values to vary freely during fitting, fits are noticeably poorer in some pH regions than others. However, we believe a less ambiguous SCM, in which fit parameters other than δ values are fairly constant (Table 2), is preferable to better individual curve fit quality.

Assumptions made during the development of the MUSIC model for use in our SCM are another source of uncertainty.

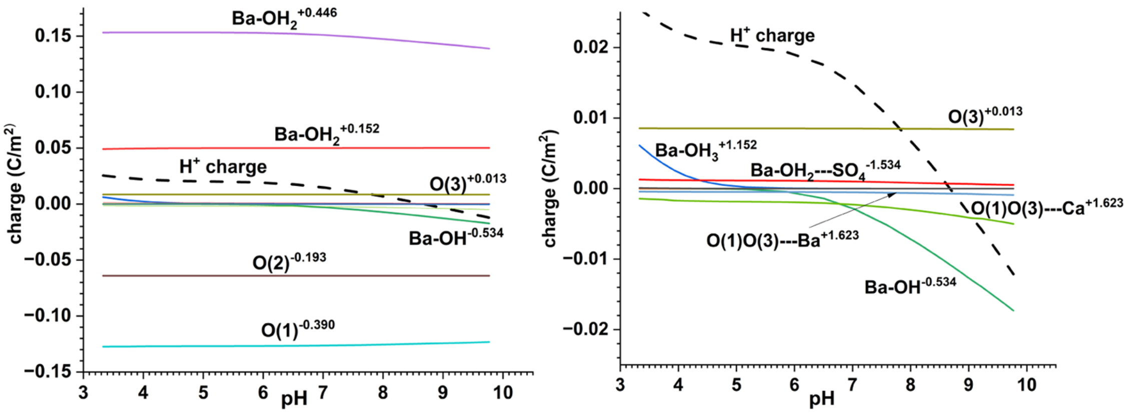

Figure 12. 25 °C, 0.03 m NaCl, and 0.001 m Ca^{2+} charge speciation. The rightmost figure enlarges the y-axis of the leftmost figure between 0.025 and −0.025 C/m^2.

First, we assumed that the (001) face of barite exclusively represents the surface of our barite powder. Although that face is certainly present (Figure 1), other faces, as well as various defect sites, are undoubtedly contributing to the observed proton uptake. However, because of the availability of in situ X-ray synchrotron results, we were at least able to utilize actual hydrated surface structures in our MUSIC model calculations rather than relying on the bulk surface structure. Second, the MUSIC model itself has inherent limitations. It is an empirically based model that nonetheless results in surface protonation constant estimates that are often in reasonable agreement with state-of-the-art molecular simulation methods such as first-principles molecular dynamics.[60] However, the model is extremely sensitive to small changes in surface bond lengths. For example, assuming an uncertainty of 5 pm in Ba−O bond lengths on the (001) surface results in an uncertainty of 4 log units in estimated protonation constant values (Table 1). Additionally, the protonation constants of the O(1), O(2), and O(3) groups would be about 4 log units greater if the number of accepting H-bonds by those groups were assumed to be one instead of two. Assigning one or two accepting H-bonds to such groups is an arbitrary choice, although one of these options generally results in a much better result when simulating proton charge data. Assuming one donating H-bond would increase the protonation constant of the O(1) group to 4.1, which is in the accessible pH range. However, preliminary modeling efforts revealed that it was not possible to differentiate the protonation constant from that of the $BaOH_2$ low group (5.38) in terms of model χ^2 values. Hence, the number of accepting H-bonds was set as two so that only the $BaOH_2$ low group contributed to proton uptake/release within the experimental pH range.

Despite these experimental and modeling uncertainties, our SCM resulted in generally acceptable fits to our proton charge and ζ-potential data, and the final set of parameters appear reasonable. δ values are generally positive (except at 15 °C) and greater at higher temperatures. Given that pretreatment consisted of at least 10 washing/decantation cycles at 50 °C, it is conceivable that higher titration temperatures were more prone to releasing residual impurities than titrations at lower temperatures. Moreover, δ values are small and all resulting H^+ charges are well within the 0.1C/m^2 uncertainty arising from a 5 pm difference in surface Ba−O bond lengths. Stern layer capacitance values are lower than those typically resulting from fitting metal oxide proton charge data (generally >0.5 F/m^2) and much lower than many earlier studies involving ionic solids such as calcite.[29,30] However, Hiemstra and Van Riemsdijk[61] have argued that the low overall Stern layer capacitance values observed for ionic solids such as AgI (∼0.2 F/m^2) result from the near dielectric saturation of water at the interface. Given that the Stern layer capacitance can be expressed as

$$C_S = \varepsilon_o \varepsilon_S / d \tag{11}$$

where ε_o = vacuum permittivity (8.854E-12 CV^{-1} m^{-1}), ε_S = Stern layer dielectric constant, and d = distance of charge separation that allows the calculation of the Stern layer dielectric constant from our SCM. Given our fit Stern layer capacitance value (∼0.25 F/m^2), along with IS adsorption height for Ba^{2+} above the (001) surface of 2.6 Å as estimated from metadynamics simulations,[11] results in a Stern layer dielectric constant of 7.3, which is near the dielectric saturation value (∼6) and suggests that water in the Stern layer is highly structured which is consistent with the barite (001) surface hydration structure observed via X-ray reflectivity.[10]

Fit protonation constants for the BaOH high and $BaOH_2$ low groups are lower than the MUSIC model estimates, but the <1.7 log K unit difference is well within uncertainty resulting from small differences in surface bond lengths. Ultimately, surface protonation constants should also be determined via molecular simulation. Barium and sulfate binding constants are dependent on the adsorption configurations assumed. Ba^{2+} (and Ca^{2+}) binding is based on a predominant observed bidentate structure,[11] while SO_4^{2-} is assumed to adsorb with the same binding constant to positively charged high and low Ba−OH groups (eqs 7−9). Distributing adsorbed Ba^{2+} and Ca^{2+} charge between the surface and Stern planes (the CD approach) did not improve fit quality. Increasing Ba^{2+} and SO_4^{2-} concentrations to barite saturation values did not change fit parameters significantly. However, the fit to the 25 °C ζ-potential data was much more dependent on the Ba^{2+} and SO_4^{2-} adsorption constants than were the proton charge data, indicating the importance of our 25 °C ζ-potential data set in constraining our SCM. Additionally, simulated solution concentrations of Ba^{2+} decrease with increasing pH consistent with the trend depicted in Figure 5. Conversely, solution SO_4^{2-} concentrations are predicted to decrease with decreasing pH due to adsorption, although we have no measurements to confirm that trend. The Ca^{2+} binding constant was manually adjusted to obtain adsorbed concentrations similar to those measured. It is conceivable that Ca^{2+} for Ba^{2+} exchange also contributes to Ca^{2+} uptake. However, since we have no information on the extent of that exchange, to reduce model ambiguity, only Ca^{2+} adsorption is included in our SCM.

Adsorbed Ba^{2+} concentrations are approximately 10 times less than those of adsorbed Ca^{2+} because its greater adsorption constant (Table 2) is outweighed by its ~100-fold lower bulk concentration. Our fit Ba^{2+} adsorption constant ($\log K \approx 4$) is similar to that obtained in the metadynamics calculations of Bracco et al.,[11] which ranged from 3.7 to 6 depending on the IS adsorbed complex considered. Their Sr^{2+} adsorption constant ($\log K = 1.8{-}3.8$) is also similar to ours for Ca^{2+} (3.0). The maximum adsorbed plus incorporated Sr^{2+} concentration found by Bracco et al.[11] at near-neutral pH was ~0.64 Sr^{2+} atoms/nm^2, although sample to sample variability was considerable. Our corresponding model results for Ca^{2+} are roughly 5 times less (~0.12 Ca^{2+} atoms/nm^2), possibly reflecting the more dissimilar size and hydration properties of Ba^{2+} and Ca^{2+} or alternatively inherent differences between the barite powder used in this study and the barite single crystals employed by Bracco et al.[11]

The predicted distribution of charged species for the 0.001 m Ca^{2+} in 0.03 m NaCl data is depicted in Figure 12. The fit (sum) H^+ charge curve is dominated by the balance between positively charged Ba high and low sites and negatively charged O(1) and O(2) sites, with the Ba high and O(1) sites being especially significant because of their higher net charges. The magnified right hand portion of Figure 12 shows that the negatively charged Ba high group dominates the net negative charge increase above pH 8, whereas the high $Ba{-}OH_3$ group accounts for the increasing proton charge below pH 5. The bidentate Ba and Ca adsorption species contribute to the net negative charge because the sum of the O(1) and O(3) group charges is negative (−0.26), whereas the adsorbed SO_4^{2-} species contribute to the net positive charge because the anchoring Ba−OH surface groups are positively charged.

As far as we are aware, the only other ionic solid study that utilizes an extensive set of potentiometric and electrophoretic mobility data to formulate a SCM is that of Villegas-Jiménez et al.[29] for gaspeite ($NiCO_3$). They applied a variety of surface complexation reactions and EDL constructs to simulate their results and concluded that a one-site, 3-pK_a, constant capacitance SCM best reproduced their proton charge and ζ-potential data, provided that the data at each ionic strength (0.001, 0.01, and 0.1 M NaCl) was modeled separately. That their SCM differs substantially from ours is not surprising. However, that their proton adsorption densities were 10 times greater than ours deserves additional investigation.

5. CONCLUSIONS

The most consequential finding of this study is the low extent of proton binding by the barite surface over the accessible pH range. Consequently, experimental uncertainties including pretreatment methods and blank corrections assume greater importance compared to metal oxides where proton binding is typically an order of magnitude greater. The low extent of proton binding led us to include a δ parameter within our SCM that allows slight vertical adjustments to the titration curves to account for uncertainty. An unforeseen consequence was that the fit δ values essentially collapsed all proton charge titration data to a narrow range of values (e.g., Figure 9), resulting in a relatively constant final set of model parameters irrespective of temperature and ionic strength (Table 2).

The final set of parameters were nonetheless constrained by ancillary experimental information, including barite (001) surface hydration structure and Ba^{2+} adsorption configurations. These constraints informed our MUSIC model surface protonation calculations as well as Ba^{2+}, Ca^{2+}, and SO_4^{2-} adsorption stoichiometries. The final set of model parameters are supported by other results. The low Stern Layer capacitance value suggests that water is close to dielectric saturation near the barite surface, which is consistent with previous X-ray reflectivity and MD simulations. Additionally, the Ba^{2+} and Ca^{2+} binding constants result in Ba^{2+} solution concentrations and adsorbed Ca^{2+} amounts similar to those determined experimentally in this study. Finally, the fit slip plane distance agrees with the established relationship between that parameter and ionic strength.

Developing SCMs which faithfully integrate macroscopic and molecular-level information for proton and ionic binding at the surfaces of ionic solids is, in many ways, more challenging than for metal oxides. Proton charge titrations, which are a mainstay of the macroscopic data available for metal oxide SCM development, are more difficult to acquire for geologically relevant ionic solids such as calcite and most other carbonates because of their high reactivity. Hence, proton charge titration data are scarce, and if our results for barite are the rule rather than the exception, the challenge will extend to accurately quantifying proton binding while accounting for high reactivity. In addition, recent studies have highlighted the roles adsorption and exchange play in the nucleation, growth, and foreign ion sequestration properties of barite.[41,62,63] The coupled processes of foreign ion adsorption and exchange, as well as synergetic uptake, and competition phenomena will be a challenge for SCMs to realistically incorporate.

The following recommendations, some of which have been previously noted by others[29,30] should help guide future investigation. Detailed attention needs to be given to solid and solution properties since differences in solid pretreatment procedures, equilibration times, and solution compositions, as well as titration methodology, may result in large differences in pH response and consequently proton uptake. This should include adequate characterization and knowledge of the specific crystal faces investigated and the possible influence of defect sites especially given the low degree of H^+ charge development observed. Additionally, both proton charge and ζ-potential titrations should be conducted on the same mineral surfaces and in the presence of a wide variety of possible adsorbates including the potential determining lattice ions. Given the low buffering capacity of barite suspensions, batch-type experiments with separate samples kept at initial differing pH values would complement the continuous proton charge titration protocol employed here. Moreover, potential adsorbate concentrations should be closely monitored during the entire titration procedure.

A broader variety of complementary molecular scale information from X-ray surface diffraction and other spectroscopic techniques, as well as molecular modeling efforts should be obtained on barite and other ionic minerals. For barite, available information primarily pertains to the (001) surface and for a limited set of experimental and simulation conditions. Moreover, except for calcite, such information for other ionic minerals is even more limited. Especially important consideration should be given to interfacial hydration structure at pristine surfaces and those containing defects, which should help better constrain SCM surface protonation and ion binding constants.

AUTHOR INFORMATION

Corresponding Author

Michael L. Machesky − *Prairie Research Institute, University of Illinois Urbana-Champaign, Champaign, Illinois 61820, United States;* orcid.org/0000-0002-8212-3922; Email: machesky@illinois.edu

Authors

Moira K. Ridley − *Department of Geosciences, Texas Tech University, Lubbock, Texas 79409, United States;* orcid.org/0000-0001-7325-9169

Frank Heberling − *Institute for Nuclear Waste Disposal, Karlsruhe Institute of Technology, 76021 Karlsruhe, Germany;* orcid.org/0000-0002-2650-2071

Johannes Lützenkirchen − *Institute for Nuclear Waste Disposal, Karlsruhe Institute of Technology, 76021 Karlsruhe, Germany;* orcid.org/0000-0002-0611-2746

Notes

The authors declare no competing financial interest.

ACKNOWLEDGMENTS

MLM acknowledges the support of the U.S. Department of Energy, Office of Science, Basic Energy Sciences, Chemical Sciences, Geosciences, and Bioscience Division. MKR acknowledges support by the National Science Foundation (CHE−1308726) and the College of Arts & Sciences Microscopy (CASM) of Texas Tech University for electron microscopy characterization. FH acknowledges partial funding via the iCross collaborative project: grant agreements 02NUK053 (German Federal Ministry of Education and Research) and SO-093 (Helmholtz association). The authors also thank Andrew Stack of Oak Ridge National Laboratory for donation of the barite powder sample and Jacquelyn Bracco of Queens College for CrystalMaker files of the hydrated barite (001) surface.

REFERENCES

(1) Bahadori, A.; Zahedi, G.; Zendehboudi, S. Estimation of potential barium sulfate (barite) precipitation in oilfield brines using a simple predictive tool. *Environ. Prog. Sustainable Energy* **2013**, *32*, 860−865.

(2) Dove, P. M.; Czank, C. A. Crystal chemical controls on the dissolution kinetics of the isostructural sulfates: Celestite, anglesite, and barite. *Geochim. Cosmochim. Acta* **1995**, *59*, 1907−1915.

(3) Zhen-Wu, B. Y.; Dideriksen, K.; Olsson, J.; Raahauge, P. J.; Stipp, S. L. S.; Oelkers, E. H. Experimental determination of barite dissolution and precipitation rates as a function of temperature and aqueous fluid composition. *Geochim. Cosmochim. Acta* **2016**, *194*, 193−210.

(4) Bosbach, D.; Hall, C.; Putnis, A. Mineral precipitation and dissolution in aqueous solution: in-situ microscopic observations on barite (001) with atomic force microscopy. *Chem. Geol.* **1998**, *151*, 143−160.

(5) Bracco, J. N.; Gooijer, Y.; Higgins, S. R. Hydrothermal atomic force microscopy observations of barite step growth rates as a function of the aqueous barium-to-sulfate ratio. *Geochim. Cosmochim. Acta* **2016**, *183*, 1−13.

(6) Kowacz, M.; Putnis, C. V.; Putnis, A. The effect of cation:anion ratio in solution on the mechanism of barite growth at constant supersaturation: Role of the desolvation process on the growth kinetics. *Geochim. Cosmochim. Acta* **2007**, *71*, 5168−5179.

(7) Stack, A. G.; Raiteri, P.; Gale, J. D. Accurate Rates of the Complex Mechanisms for Growth and Dissolution of Minerals Using a Combination of Rare-Event Theories. *J. Am. Chem. Soc.* **2012**, *134*, 11−14.

(8) Ruiz-Agudo, C.; Putnis, C. V.; Ruiz-Agudo, E.; Putnis, A. The influence of pH on barite nucleation and growth. *Chem. Geol.* **2015**, *391*, 7−18.

(9) Allan, N. L.; Rohl, A. L.; Gay, D. H.; Catlow, C. R. A.; Davey, R. J.; Mackrodt, W. C. Calculated bulk and surface properties of sulfates. *Faraday Discuss.* **1993**, *95*, 273−280.

(10) Bracco, J. N.; Lee, S. S.; Stubbs, J. E.; Eng, P. J.; Heberling, F.; Fenter, P.; Stack, A. G. Hydration Structure of the Barite (001)−Water Interface: Comparison of X-ray Reflectivity with Molecular Dynamics Simulations. *J. Phys. Chem. C* **2017**, *121*, 12236−12248.

(11) Bracco, J. N.; Lee, S. S.; Stubbs, J. E.; Eng, P. J.; Jindra, S.; Warren, D. M.; Kommu, A.; Fenter, P.; Kubicki, J. D.; Stack, A. G. Simultaneous Adsorption and Incorporation of Sr2+ at the Barite (001)−Water Interface. *J. Phys. Chem. C* **2019**, *123*, 1194−1207.

(12) Bracco, J. N.; Lee, S. S.; Braha, I.; Dorfman, A.; Fenter, P.; Stack, A. G. Pb Sorption at the Barite (001)−Water Interface. *J. Phys. Chem. C* **2020**, *124*, 22035−22045.

(13) Weber, J.; Bracco, J. N.; Yuan, K.; Starchenko, V.; Stack, A. G. Studies of Mineral Nucleation and Growth Across Multiple Scales: Review of the Current State of Research Using the Example of Barite (BaSO4). *ACS Earth Space Chem.* **2021**, *5*, 3338−3361.

(14) Stumm, W.; Huang, C. P.; Jenkins, S. R. Specific Chemical Interaction Affecting the Stability of Dispersed Systems. *Croat. Chem. Acta* **1970**, *42*, 223−245.

(15) Schindler, P. W.; Gamsjäger, H. Acid — base reactions of the TiO2 (Anatase) — water interface and the point of zero charge of TiO2 suspensions. *Kolloid Z. Z. Polym.* **1972**, *250*, 759−763.

(16) Dzombak, D. A.; Morel, F. M. M. *Surface Complexation Modeling: Hydrous Ferric Oxide*; Wiley, 1991.

(17) Westall, J.; Hohl, H. A comparison of electrostatic models for the oxide/solution interface. *Adv. Colloid Interface Sci.* **1980**, *12*, 265−294.

(18) Zhang, Z.; Fenter, P.; Cheng, L.; Sturchio, N. C.; Bedzyk, M. J.; Předota, M.; Bandura, A.; Kubicki, J. D.; Lvov, S. N.; Cummings, P. T.; Chialvo, A. A.; Ridley, M. K.; Bénézeth, P.; Anovitz, L.; Palmer, D. A.; Machesky, M. L.; Wesolowski, D. J. Ion Adsorption at the Rutile−Water Interface: Linking Molecular and Macroscopic Properties. *Langmuir* **2004**, *20*, 4954−4969.

(19) Hiemstra, T.; Van Riemsdijk, W. H. On the relationship between charge distribution, surface hydration, and the structure of the interface of metal hydroxides. *J. Colloid Interface Sci.* **2006**, *301*, 1−18.

(20) Peacock, C. L.; Sherman, D. M. Copper(II) sorption onto goethite, hematite and lepidocrocite: a surface complexation model based on ab initio molecular geometries and EXAFS spectroscopy. *Geochim. Cosmochim. Acta* **2004**, *68*, 2623−2637.

(21) Mendez, J. C.; Hiemstra, T. High and low affinity sites of ferrihydrite for metal ion adsorption: Data and modeling of the alkaline-earth ions Be, Mg, Ca, Sr, Ba, and Ra. *Geochim. Cosmochim. Acta* **2020**, *286*, 289−305.

(22) Ridley, M. K.; Machesky, M. L.; Kubicki, J. D. Experimental Study of Strontium Adsorption on Anatase Nanoparticles as a Function of Size with a Density Functional Theory and CD Model Interpretation. *Langmuir* **2015**, *31*, 703−713.

(23) Van Cappellen, P.; Charlet, L.; Stumm, W.; Wersin, P. A surface complexation model of the carbonate mineral-aqueous solution interface. *Geochim. Cosmochim. Acta* **1993**, *57*, 3505−3518.

(24) Pokrovsky, O. S.; Schott, J.; Thomas, F. Dolomite surface speciation and reactivity in aquatic systems. *Geochim. Cosmochim. Acta* **1999**, *63*, 3133−3143.

(25) Charlet, L.; Wersin, P.; Stumm, W. Surface charge of MnCO3and FeCO3. *Geochim. Cosmochim. Acta* **1990**, *54*, 2329−2336.

(26) Bonto, M.; Eftekhari, A. A.; Nick, H. M. Electrokinetic behavior of artificial and natural calcites: A review of experimental measurements and surface complexation models. *Adv. Colloid Interface Sci.* **2022**, *301*, No. 102600.

(27) Eriksson, R.; Merta, J.; Rosenholm, J. B. The calcite/water interface: I. Surface charge in indifferent electrolyte media and the influence of low-molecular-weight polyelectrolyte. *J. Colloid Interface Sci.* **2007**, *313*, 184−193.

(28) Eriksson, R.; Merta, J.; Rosenholm, J. B. The calcite/water interface II. Effect of added lattice ions on the charge properties and adsorption of sodium polyacrylate. *J. Colloid Interface Sci.* **2008**, *326*, 396−402.

(29) Villegas-Jiménez, A.; Mucci, A.; Pokrovsky, O. S.; Schott, J. Acid−Base Behavior of the Gaspeite (NiCO3(s)) Surface in NaCl Solutions. *Langmuir* **2010**, *26*, 12626−12639.

(30) Wolthers, M.; Charlet, L.; Van Cappellen, P. The surface chemistry of divalent metal carbonate minerals; a critical assessment of surface charge and potential data using the charge distribution multi-site ion complexation model. *Am. J Sci.* **2008**, *308*, 905−941.

(31) Wolthers, M.; Di Tommaso, D.; Du, Z.; de Leeuw, N. H. Calcite surface structure and reactivity: molecular dynamics simulations and macroscopic surface modelling of the calcite−water interface. *Phys. Chem. Chem. Phys.* **2012**, *14*, 15145−15157.

(32) Heberling, F.; Bosbach, D.; Eckhardt, J.-D.; Fischer, U.; Glowacky, J.; Haist, M.; Kramar, U.; Loos, S.; Müller, H. S.; Neumann, T.; Pust, C.; Schäfer, T.; Stelling, J.; Ukrainczyk, M.; Vinograd, V.; Vučak, M.; Winkler, B. Reactivity of the calcite−water-interface, from molecular scale processes to geochemical engineering. *Appl. Geochem.* **2014**, *45*, 158−190.

(33) Heberling, F.; Klačić, T.; Raiteri, P.; Gale, J. D.; Eng, P. J.; Stubbs, J. E.; Gil-Díaz, T.; Begović, T.; Lützenkirchen, J. Structure and Surface Complexation at the Calcite(104)−Water Interface. *Environ. Sci. Tech.* **2021**, *55*, 12403−12413.

(34) Hang, J. Z.; Zhang, Y. F.; Shi, L. Y.; Feng, X. Electrokinetic properties of barite nanoparticles suspensions in different electrolyte media. *J Mater. Sci.* **2007**, *42*, 9611−9616.

(35) Mohammed, I.; Al Shehri, D. A.; Mahmoud, M.; Kamal, M. S.; Alade, O. Surface Charge Investigation of Reservoir Rock Minerals. *Energy Fuels* **2021**, *35*, 6003−6021.

(36) Buchanan, A. S.; Heymann, E. The electrokinetic potential of barium sulfate. *Proc. R. Soc. London, Ser. A* **1948**, *195*, 150−162.

(37) Zhang, X.; Du, H.; Wang, X.; Miller, J. D. Surface chemistry considerations in the flotation of rare-earth and other semisoluble salt minerals. *Min., Metall., Explor.* **2013**, *30*, 24−37.

(38) Bokern, D. G.; Hunter, K. A.; McGrath, K. M. Charged Barite−Aqueous Solution Interface: Surface Potential and Atomically Resolved Visualization. *Langmuir* **2003**, *19*, 10019−10027.

(39) Ridley, M. K.; Hackley, V. A.; Machesky, M. L. Characterization and Surface-Reactivity of Nanocrystalline Anatase in Aqueous Solutions. *Langmuir* **2006**, *22*, 10972−10982.

(40) Ridley, M. K.; Hiemstra, T.; van Riemsdijk, W. H.; Machesky, M. L. Inner-sphere complexation of cations at the rutile−water interface: A concise surface structural interpretation with the CD and MUSIC Model. *Geochim. Cosmochim. Acta* **2009**, *73*, 1841−1856.

(41) Tokunaga, K.; Takahashi, Y. Effective Removal of Selenite and Selenate Ions from Aqueous Solution by Barite. *Environ. Sci. Technol.* **2017**, *51*, 9194−9201.

(42) Parkhurst, D. L.; Appelo, C. A. J. *Description of Input and Examples for Phreeqc Version 3: A Computer Program for Speciation, Batch-reaction, One-dimensional Transport, and Inverse Geochemical Calculations*; US Geological Survey Techniques and Methods: Reston, 2013.

(43) Felmy, A. R.; Rai, D.; Amonette, J. E. The Solubility of Barite and Celestite in Sodium Sulfate: Evaluation of Thermodynamic Data. *J. Solution Chem.* **1990**, *19*, 175−185.

(44) Poeter, E. P.; Hill, M. C. *Documentation of UCODE, a Computer Code for Universal Inverse Modeling*, Diane Publishing: 1998.

(45) Hiemstra, T.; Venema, P.; Van Riemsdijk, W. H. Intrinsic proton affinity of reactive surface groups of metal (hydr) oxides: The bond valence principle. *J. Colloid Interface Sci.* **1996**, *184*, 680−692.

(46) Jacobsen, S. D.; Smyth, J. R.; Swope, R. J.; Downs, R. T. Rigid-body character of the SO4 groups in celestine, anglesite and barite. *Can. Mineral.* **1998**, *36*, 1053−1060.

(47) Brown, I. D. *The Chemical Bond in Inorganic Chemistry: the Bond Valence Model*; Oxford University Press, 2016; Vol. *27*.

(48) Machesky, M. L.; Wesolowski, D. J.; Palmer, D. A.; Ridley, M. K. On the temperature dependence of intrinsic surface protonation equilibrium constants: an extension of the revised MUSIC model. *J. Colloid Interface Sci.* **2001**, *239*, 314−327.

(49) Machesky, M. L.; Predota, M.; Wesolowski, D. J.; Vlcek, L.; Cummings, P. T.; Rosenqvist, Jr.; Ridley, M. K.; Kubicki, J. D.; Bandura, A. V.; Kumar, N.; Sofo, J. O. Surface protonation at the rutile (110) interface: explicit incorporation of solvation structure within the refined MUSIC model framework. *Langmuir* **2008**, *24*, 12331−12339.

(50) Hiemstra, T.; Yong, H.; Van Riemsdijk, W. H. Interfacial charging phenomena of aluminum (hydr) oxides. *Langmuir* **1999**, *15*, 5942−5955.

(51) Fedkin, M. V.; Zhou, X. Y.; Kubicki, J. D.; Bandura, A. V.; Lvov, S. N.; Machesky, M. L.; Wesolowski, D. J. High Temperature Microelectrophoresis Studies of the Rutile/Aqueous Solution Interface. *Langmuir* **2003**, *19*, 3797−3804.

(52) Adams, F. T.; Machesky, M. L.; Kabengi, N. Surface Complexation Modeling Approach for Aluminum-Substituted Ferrihydrites. *ACS Earth Space Chem.* **2021**, *5*, 1355−1362.

(53) Lützenkirchen, J.; Preočanin, T.; Kallay, N. A macroscopic water structure based model for describing charging phenomena at inert hydrophobic surfaces in aqueous electrolyte solutions. *Phys. Chem. Chem. Phys.* **2008**, *10*, 4946−4955.

(54) Leroy, P.; Tournassat, C.; Bizi, M. Influence of surface conductivity on the apparent zeta potential of TiO2 nanoparticles. *J. Colloid Interface Sci.* **2011**, *356*, 442−453.

(55) Barišić, A.; Lützenkirchen, J.; Bebić, N.; Li, Q.; Hanna, K.; Shchukarev, A.; Begović, T. Experimental Data Contributing to the Elusive Surface Charge of Inert Materials in Contact with Aqueous Media. *Colloids Interfaces* **2021**, *5*, No. 6.

(56) Al Mahrouqi, D.; Vinogradov, J.; Jackson, M. D. Zeta potential of artificial and natural calcite in aqueous solution. *Adv. Colloid Interface Sci.* **2017**, *240*, 60−76.

(57) Předota, M.; Machesky, M. L.; Wesolowski, D. J. Molecular Origins of the Zeta Potential. *Langmuir* **2016**, *32*, 10189−10198.

(58) Preočanin, T.; Selmani, A.; Lindqvist-Reis, P.; Heberling, F.; Kallay, N.; Lützenkirchen, J. Surface charge at Teflon/aqueous solution of potassium chloride interfaces. *Colloids Surf., A* **2012**, *412*, 120−128.

(59) Lützenkirchen, J.; Preočanin, T.; Kovačević, D.; Tomišić, V.; Lövgren, L.; Kallay, N. Potentiometric titrations as a tool for surface charge determination. *Croat. Chem. Acta* **2012**, *85*, 391−417.

(60) Zhang, Y.; Liu, X.; Cheng, J.; Lu, X. Interfacial structures and acidity constants of goethite from first-principles Molecular Dynamics simulations. *Am. Mineral.* **2021**, *106*, 1736−1743.

(61) Hiemstra, T.; Van Riemsdijk, W. H. Physical chemical interpretation of primary charging behaviour of metal (hydr) oxides. *Colloids Surf.* **1991**, *59*, 7−25.

(62) Yang, P.; Rampal, N.; Weber, J.; Bracco, J. N.; Fenter, P.; Stack, A. G.; Lee, S. S. Synergistic Enhancement of Lead and Selenate Uptake at the Barite (001)−Water Interface. *Environ. Sci. Technol.* **2022**, *56*, 16801−16810.

(63) Deng, N.; Zuo, X.; Stack, A. G.; Lee, S. S.; Zhou, Z.; Weber, J.; Hu, Y. Selenite and Selenate Sequestration during Coprecipitation with Barite: Insights from Mineralization Processes of Adsorption, Nucleation, and Growth. *Environ. Sci. Technol* **2022**, *56*, 15518−15527.